



TITLE:

On the application of differential phase measurements to study the zonal large scale wave structure (LSWS) in the ionospheric electron content

AUTHOR(S):

Tulasi Ram, S.; Yamamoto, M.; Tsunoda, R. T.;
Thampi, S. V.; Gurubaran, S.

CITATION:

Tulasi Ram, S. ...[et al]. On the application of differential phase measurements to study the zonal large scale wave structure (LSWS) in the ionospheric electron content. Radio Science 2012, 47(2): RS2001.

ISSUE DATE:

2012-03

URL:

<http://hdl.handle.net/2433/154852>

RIGHT:

©2012. American Geophysical Union.; この論文は出版社版ではありません。引用の際には出版社版をご確認ご利用ください。; This is not the published version. Please cite only the published version.

1 On the application of differential phase measurements to study the zonal 2 large scale wave structure (LSWS) in the ionospheric electron content

3 S. Tulasi Ram^{1,2}, M. Yamamoto¹, R. T. Tsunoda³, S. V. Thampi⁴ and S. Gurubaran²

4 ¹RISH, Kyoto University, Uji, Kyoto, Japan

5 ²Equatorial Geophysical Research Laboratory, Indian Institute of Geomagnetism, Tirunelveli, India

6 ³Center for Geospace Studies, SRI International, Menlo Park, California

7 ⁴Physical Research Laboratory, Ahmedabad, India

8

9 **Abstract:** The GNU Radio Beacon Receiver (GRBR) Network has been recently established to provide
10 coverage of Southeast Asia and Pacific low-latitude regions, with planned extensions into the Indian and
11 African longitude sectors. With the availability of CERTO (Coherent Electromagnetic Radio
12 Tomography) beacon transmissions from Communication/Navigation Outage Forecasting System
13 (C/NOFS) satellite, which is in a unique low-inclination (13°) orbit, it is now possible to study zonal large
14 scale wave structure (LSWS) in ionospheric total electron content (TEC) with fine spatial resolution over
15 a wide longitudinal region. An automated procedure to determine absolute TEC from relative TEC
16 measurements for low inclination CNOFS orbits has been implemented through a simple single station
17 procedure for initial offset estimation, which is shown to be consistent with the better established two
18 station method [Leitinger et al., 1975] and with observations from a Digisonde. The LSWS is extracted
19 by subtracting the background variation from longitudinal variation of TEC. The upwellings of LSWS
20 manifest as depletions in the residual TEC variations. Further, these zonal structures have been found, in
21 general, to be aligned with geomagnetic (\vec{B}) field lines, and the scintillation patches have been found to
22 align with the west walls of TEC depletions. This spatial alignment recapitulates the premise that the
23 observed zonal wave-like structures in TEC are the manifestations of bottom side LSWS. Hence, the
24 methodology presented in this paper, would prove useful in future, to study the characteristics of LSWS
25 on a regular basis.

26

27 1. Introduction

28 The dual-frequency, differential phase measurements from low earth orbiting satellites (LEOS)
29 have been extensively used to study the ionospheric total electron content (TEC) from the beginning of
30 the space era (Aitchison and Weeks, 1959; Garriot, 1960; Davis, 1980). Since the majority of LEOS that
31 transmitted beacon signals in the past were polar (or high inclination) orbiting satellites, this technique
32 has been widely used to study the latitudinal variation of TEC as well as tomographic imaging of latitude-
33 altitude structure of ionospheric electron density along a given meridian. Clearly, if beacon transmitters
34 are available on LEOS in low inclination orbits, it would be possible to derive the zonal variation of TEC
35 as a function of longitude over a wide region with fine spatial resolution. In this scenario, C/NOFS is the
36 first and the only LEOS with beacon transmitter onboard in the near-equatorial (13° inclination) orbit, and
37 therefore, it provides an excellent opportunity to measure the zonal structures in TEC over equatorial and
38 low latitudes.

39 The launch of C/NOFS is very opportune because of high space weather interest, particularly, on
40 the topic of equatorial spread-F (ESF), for example to explore the initial seed processes that lead to the
41 evolution of equatorial plasma bubbles (EPBs) that cause scintillations. There is accumulating evidence
42 that the zonal large scale wave structure (LSWS) in the bottom side F-region provides a basis for initial
43 development of ESF [Tsunoda 1981; Tsunoda and White 1981]. These zonal structures together with pre-
44 reversal enhancement of eastward electric field (PRE) appear to control the location and onset of ESF
45 [Tsunoda and White 1981; Tsunoda 2005, 2008; Tsunoda et al. 2010; Saito and Maruyama, 2007;
46 Thampi et al. 2009; Abdu et al. 2009 and Kherani et al. 2009]. However, these studies are mostly case
47 studies and general consensus about the role of LSWS on the occurrence of ESF has not yet emerged,
48 primarily, due to lack of statistically significant number of observations. A reason for the dearth in
49 observations of LSWS has been the inability to detect and characterize LSWS properties with currently
50 available instruments, except by ALTAIR radar, a steerable incoherent scatter radar in Kwajalein Atoll.

51 In this paper, we describe the application of differential phase technique to derive the zonal
52 LSWS from the CERTO beacon transmissions of C/NOFS [Bernhardt and Siefring, 2006]. This method,
53 for the first time, provides a simple and inexpensive means for studying the physics of these zonal
54 structures, and should also be useful in the future, if and when more low-inclination beacon satellites
55 become available.

56 2. GRBR Network

57 A network of radio beacon receivers, namely GNU Radio Beacon Receiver (GRBR) Network,
58 has been recently established to provide coverage of the low-latitude region. At present, GRBRs are
59 operating in the Southeast Asia and Pacific region, with planned extensions into the other longitude
60 sectors. A few have already been installed in Africa and others are planned for Indian region. The
61 scientific objectives of this network are many such as three dimensional tomographic imaging of
62 ionosphere, investigations of ionospheric scintillations and study of middle-upper atmospheric coupling
63 processes leading to ESF. However, the scope of the present report is only confined to characterize the
64 LSWS using radio beacon transmissions from C/NOFS. The GRBR is a compact and software controlled
65 digital receiver optimally designed (unlike the commercially available analog receivers) to track two or
66 more satellites simultaneously to ensure the lossless reception from all the satellites passes that are in the
67 field of view of the receiving antenna. This is achieved by multi-channel reception and careful
68 scheduling procedures of GRBR system. To avoid multi-path effects, we have set a lower limit of 20°
69 satellite elevation angle for data acquisition. The distribution of beacon receivers is shown in Figure 1
70 and their station names, codes (referred in this paper) along with their geographical locations are given in
71 Table 1. The detailed circuitry of the receiving system and the method of TEC measurement employed in
72 GRBR system were reported by Yamamoto, [2008]. Further, the details of system design and software
73 codes are open to the community at the URL <http://www.rish.kyoto-u.ac.jp/digitalbeacon/>.

74

75

76 3. Estimation of Absolute TEC

77 To extract the zonal LSWS, an accurate determination of absolute TEC and its variation as a
78 function of longitude is very important. A discussion of various techniques for estimation of absolute
79 TEC has been presented by Bernhardt et al. [2010]. Since the ionosphere is a dispersive medium, a radio
80 wave passing through the ionosphere experiences an amount of group delay and phase advance that
81 depends on the operating frequency. When two radio waves with different frequencies are transmitted,
82 the phase difference (Φ) between the two received signals is proportional to the TEC along the line-of-
83 sight path from the transmitter to receiver. An example of using differential group delay to obtain TEC
84 can be found in Tsunoda and Towle [1979]. The most commonly used satellite radio beacon frequencies
85 have been 150 and 400 MHz, whose ratio is 3:8. For example, two radio waves at $f_1 = q_1 f_r$ and $f_2 = q_2 f_r$
86 (in a ratio of $q_1:q_2$ of a common frequency f_r) are used and their phases at the receiving end are ϕ_1 and ϕ_2 ,
87 then the phase difference Φ is given by

$$88 \quad \Phi = \frac{\phi_2}{q_2} - \frac{\phi_1}{q_1} = \frac{40.3}{f_r c} \left[\frac{1}{q_2^2} - \frac{1}{q_1^2} \right] \int N dx \quad \text{--- (1)}$$

89 Here, $\int N dx$ is the slant (line-of-sight) TEC and c is the speed of light. The unit for TEC is generally
90 expressed as TEC units (1 TECu = 10^{16} electrons/m²). If it is assumed that the state of the ionosphere
91 does not change significantly within the duration of a typical satellite pass (~ 10 – 12 minutes), the
92 derived TEC variation can be assumed to be a function of satellite position. For LEOS in equatorial (or
93 low inclination) orbits such as C/NOFS, the TEC can be derived as a function of longitude. Since the
94 phase counting in the receiver begins from the time when the receiver acquires the phase lock with the
95 signal, the measured phase of the radio wave at the receiver is already advanced by an unknown integer
96 multiples of 2π through the ionosphere which will introduce an unknown initial TEC offset (Ψ). Hence,
97 the measured TEC is only a relative variation of slant TEC (S_r) along the direction of satellite pass. Once
98 the unknown initial TEC offset (Ψ) is estimated, the absolute value of vertical TEC can be obtained from

$$99 \quad V_a = (S_r + \Psi) \cdot \cos \chi \quad \text{--- (2)}$$

100 where V_a is the absolute vertical TEC, S_r is the relative slant TEC, Ψ is the unknown TEC offset and χ is
101 the satellite zenith angle at ionospheric pierce point (IPP) height. Denoting $S_r \cos\chi = V_r$ (relative vertical
102 TEC), then equation (2) becomes,

$$103 \quad V_r = V_a - \Psi \cos\chi \quad \text{---} \quad (3)$$

104 It should be mentioned here that the equations (2) and (3) hold only during the time spans when the
105 phases of the two radio waves have been observed continuously without any signal loss. In case of phase
106 slips occur due to signal loss, a new Ψ must generally be used. However, these phase slips are
107 automatically detected and resolved by appropriately shifting the slant TEC curves during the
108 preprocessing of the data. Thus, the remaining problem in evaluating the absolute vertical TEC is the
109 determination of initial TEC offset, Ψ .

110 3.1 Leitinger's two station method

111 A widely used practice for the estimation of Ψ , using the simultaneous observations from two or
112 more closely spaced stations, was originally proposed by Leitinger et al., [1975]. When the two closely
113 spaced receivers track the same satellite, it is possible that a region at the mean IPP height can be
114 observed from both receivers (i.e., region of overlap). At a given location within the overlapping region,
115 the ionospheric pierce points from the two receivers should be as close as possible. For polar/equatorial
116 orbiting satellites, the stations should be aligned along the same longitudinal/latitude (in other words, the
117 longitudinal/latitudinal separation of the stations should be as small as possible). Then, it is reasonable to
118 assume that the absolute vertical TEC (V_a) from each receiver is same at that IPP location

$$119 \quad \text{i.e.,} \quad V_{a1} = V_{a2} \quad \text{---} \quad (4)$$

120 The difference between the V_{a1} and V_{a2} should be negligible when the horizontal gradient in TEC is not
121 too large. In this case, the vertical electron density distribution should be nearly independent of
122 horizontal distance in the vicinity of IPP location (Leitinger et al., 1975).

123 Then from (3) $V_{r1} + \Psi_1 \cos\chi_1 = V_{r2} + \Psi_2 \cos\chi_2$

124 or $V_{r1} - V_{r2} = \Psi_2 \cdot \cos \chi_2 - \Psi_1 \cdot \cos \chi_1$ --- (5)

125 Similarly, for n number of IPP locations within the overlapping region, one can get a system of n
126 equations (similar to equation (5)) with different χ_1 and χ_2 as independent variables and V_{r1} and V_{r2} as
127 dependent variables, which can be solved by least squares fit to obtain the unknown constants Ψ_1 and Ψ_2
128 for the two stations. Similar procedure can be extended when the observations from more than two
129 receivers are simultaneously available [Kersley et al. 1993].

130 3.2 Single station method for C/NOFS passes

131 For low inclination satellite passes, such as C/NOFS, the TEC variation as function of satellite
132 position is mainly the longitudinal variation primarily due to local time or solar zenith angle variation. In
133 addition, small variation in latitude ($\sim 3 - 4^\circ$ for a typical pass) also introduces a gradient in the observed
134 TEC due to the presence of Equatorial Ionization Anomaly (EIA) at low latitudes. In the presence of
135 slowly varying ionosphere, the ionosphere itself can be considered as frozen for the duration of satellite
136 pass (about ~ 10 -12 minutes). Thus, it is reasonable to assume, for the first order, that the V_a varies quasi-
137 linearly with horizontal distance. Consider that the station is at the origin of a Cartesian coordinate
138 system in which x is eastward (zonal), y is northward and z is upward. Then the linear variation of V_a in
139 zonal direction is given by,

140 $V_a = V_a^{\chi_c} + m \cdot x$ --- (6),

141 where χ_c is the satellite zenith angle at the closest approach. Assuming that the satellite orbits in the x -
142 direction and the height of ionospheric pierce point is h , we have

143 $\tan \chi = d/h$ --- (7),

144 where d is the radial ground distance of ionospheric pierce point (IPP). If we define the northward
145 ground distance of IPP at the closest approach to be y_0 at $x=0$, then

146 $\tan \chi_c = y_0/h$ --- (8)

147 Replacing y_0 in (7),

$$148 \quad \tan \chi = \frac{\sqrt{x^2 + y_0^2}}{h} = \frac{\sqrt{x^2 + h^2 \cdot \tan^2 \chi_c}}{h} \quad \text{---} \quad (9)$$

149 Solving for x ,

$$150 \quad x = h \cdot [\tan^2 \chi - \tan^2 \chi_c]^{\frac{1}{2}} \quad \text{---} \quad (10)$$

151 substituting (10) in (6),

$$152 \quad V_a = V_a^{\chi = \chi_c} + m \cdot h \cdot [\tan^2 \chi - \tan^2 \chi_c]^{\frac{1}{2}} \quad \text{---} \quad (11)$$

153 substituting (11) in (3)

$$154 \quad V_r = V_a^{\chi = \chi_c} + m \cdot h \cdot [\tan^2 \chi - \tan^2 \chi_c]^{\frac{1}{2}} - \Psi \cdot \cos \chi \quad \text{---} \quad (12)$$

155 Now, the system of n equations similar to (12) with n number of χ values as an independent variables and
156 V_r as a dependent variables, can be solved for Ψ and m by nonlinear least squares fitting. The weighted
157 least squares fitting is used with bi-square weighting where the data points with high elevation angle are
158 given more weight and the outliers far from the fitted line are given less weightage.

159 Figure 2 shows the comparison of V_a estimated from both methods for two of C/NOFS orbits at
160 0949 and 1459 UT on March 9, 2011 over the stations Bac Lieu (BCL) and Ho Chi Minh City (HCM).
161 The top panels show the line-of-sight TEC measured at the two stations (BCL and HCM) as a function of
162 longitudes corresponding to an ionospheric pierce point (IPP) altitude of 300 km. Note that although the
163 TEC variation is presented as a function of IPP longitude, its actual variation is along the IPP track that
164 includes the latitudinal variation (though small) as well. The middle panels show the V_a derived from the
165 observations over BCL and HCM by single station method (blue and red solid lines for BCL and HCM,
166 respectively) and two stations method (green and brown dotted lines for BCL and HCM, respectively).
167 Bottom panels show the amplitude scintillations observed at 150 MHz (blue) and 400 MHz (red)
168 frequency radio beacon signals. It can be observed from this figure (middle panels) that the estimated V_a

169 by the two methods are very close to each other for the C/NOFS pass at 0949 UT, indicating the TEC
 170 offset estimate (Ψ) by single station method is consistent with two-station method. However, for the
 171 C/NOFS pass at 1459 UT, the estimated values of Ψ by two-station method are much larger (50.74 and
 172 55.28 TECu) than those obtained by single-station method (23.27 and 25.29 TECu). As can be seen
 173 from the figure, these larger values of Ψ obtained in two-station method manifest as an artificial
 174 enhancement in V_a over the region of closest approach due to multiplication with a factor of $\cos \chi$
 175 (equation (2)). This discrepancy between the two methods is mainly due to fluctuations in S_r around 107
 176 - 118° longitudes associated with scintillation as can be seen from the bottom panels. With a view to
 177 further examine the effect of scintillations on the two station method, the TEC offsets for BCL and HCM
 178 are computed by carefully selecting the region of overlap to 92 – 102°E longitudes i.e., confining only to
 179 the region where the TEC observations are not affected by the scintillation. Interestingly, the resultant
 180 values for Ψ and the absolute TEC (blue and red dotted lines for BCL and HCM, respectively) are quite
 181 close to those obtained by single station method. This clearly indicates that the estimated V_a from both
 182 the methods are consistent when the measured S_r was not affected by the scintillation.

183 It should be mentioned here that both these methods have some limitations. The single station
 184 method is subject to the assumption that the ionospheric TEC varies linearly with horizontal distance.
 185 The longitudinal extent of observation for one satellite pass is typically ~30 - 35°. Over this horizontal
 186 distance, the principal source of variation in TEC arises from the local time variation of about 2 to 2.3
 187 hours which can be assumed, in the first order, to be a linear variation. Further, a small latitudinal
 188 distance (3 – 4°) covered by the satellite pass also introduces a horizontal variation in TEC due to the
 189 presence of Equatorial Ionization Anomaly (EIA) over the low latitudes. The other sources for horizontal
 190 variation in TEC may come from the presence of ESF irregularities/plasma bubbles, medium scale
 191 travelling ionospheric disturbances, large scale wave structures, altitudinal variation of C/NOFS orbit, etc.
 192 Therefore, it is possible that the non-linear variations introduced by the various sources are superimposed
 193 on a mean linear variation in TEC introduced by the local time/solar zenith angle variation. During our

194 analysis for many satellite passes by solving the equation (12) by least squares fit, it is observed that the
 195 estimated coefficients (Ψ and m) are more dependent on the mean variation of TEC (trend) over the full
 196 data length and are less sensitive to the smaller scale non-linear variations. However, the estimation of Ψ
 197 becomes ambiguous when the major portion of line-of-sight TEC data is severely affected by the
 198 scintillations. On the other hand, the two station method depends on the assumption of equality of V_a at a
 199 given IPP in the overlapping region observed by the two receivers that are separated horizontally. When
 200 the horizontal gradient of ionospheric TEC is significantly large, the line-of-sight paths between the
 201 transmitter and receivers for different stations pass through the regions with different electron densities,
 202 and hence, the assumption of equality is violated. Therefore, the estimated value for Ψ is highly sensitive
 203 to the selection of overlapping region and often is unrealistic when the gradients are large in the
 204 overlapping region, such as due to local time variation, EIA and the presence of ESF irregularities. For
 205 the low-inclination orbiting satellite passes, such as C/NOFS, the longitudinal gradients of TEC is
 206 significant owing to the solar zenith angle variation which maximizes during the sunrise and sunset
 207 periods. Given that the resultant offset estimates by single station method are consistent with those by
 208 two station method, the single station method is invulnerable when the horizontal gradients are linear.
 209 Moreover, the single station approach is simple and practicable when the closely spaced receivers are not
 210 available. However, this method may not be suitable to derive the absolute TEC from polar (or high
 211 inclination) orbiting satellites, particularly at low latitudes, due to large gradients associated with double
 212 humped latitudinal variation of TEC introduced by EIA.

213 3.3 Validation of single station method

214 Figure 3 shows the longitudinal variation of V_a by single station method during nine successive
 215 C/NOFS orbits from 0815 UT to 2206 UT on May 18, 2011 over an equatorial station, Kosrae (KOS).
 216 The x-axis for each panel is shown in terms of local times and the corresponding longitudes are presented
 217 in the axis at top. It can be observed from this figure that the longitudinal variations of TEC in each panel
 218 are in the right sense with the local time variation, particularly, for those passes where the observations

219 crossing the sunset and sunrise solar terminators (at 0815 UT and 1837 UT). Further, the V_a at any
 220 selected longitude is also found to decrease as the local time advances in to midnight and post-midnight
 221 hours and increases after sunrise. For example, consider a longitude at 167.2°E and the estimated V_a for
 222 the nine successive orbits are plotted as a function of local time (blue curve with open circles) in Figure
 223 4b. This longitude sector is selected because of the availability of a Digisonde at Kwajalein (KWA) for
 224 validating the estimated TEC. The tracks of ionospheric pierce points (at 300 km) for the nine orbits are
 225 numbered 1 to 9 and the locations of KOS and KWA are shown in Figure 4a. It can be seen that the V_a
 226 exhibits a clear local time variation with decrease after sunset, reaching a minimum around 0415 LT and
 227 increase after sunrise.

228 In order to validate the estimated V_a , the vertical electron density profiles are reconstructed up to
 229 the altitude of C/NOFS orbit by assimilating the topside in-situ ion density measurements from C/NOFS
 230 Ion Velocity Meter (IVM) [Coley et al, 2010] with the bottom side profiles obtained from the Digisonde.
 231 In this method, the topside ion density data points are used as an anchor point to reconstruct the topside
 232 profile using α -Chapman function which is found to be in good agreement with the incoherent scatter
 233 radar profiles and the detailed procedure can be found in Tulasi Ram et al., [2009]. Integrating these
 234 vertical profiles provide the vertical TEC over the KWA (herein after called as ITEC) between the ground
 235 and the C/NOFS altitude and are plotted as red curve with asterisks in Figure 4b. It should be mentioned
 236 here that the V_a from beacon data (blue curve) corresponds to 167.2°E IPP longitude for all the nine
 237 C/NOFS orbits but their IPP latitudes differ for each orbit. Whereas the ITEC (red curve) can be
 238 considered as a vertical TEC over KWA since the bottom side density profile is obtained from the
 239 Digisonde at KWA. However, the topside anchor points of in-situ data corresponds to different latitudes
 240 for the nine C/NOFS orbits. Thus, the ITEC represents the true vertical TEC over KWA between the
 241 ground to C/NOFS altitude only when C/NOFS orbit is in close latitudinal proximity of KWA Digisonde.
 242 The horizontal distance between the observational locations of V_a and KWA are plotted as vertical bars
 243 with right hand side scale in Figure 4b. Therefore, the estimated V_a is expected to be close to true TEC

244 only when the horizontal distance is small. It can be seen from this figure that the V_a is close to true TEC
245 during 0 to 6 LT, i.e., for passes numbered 4, 5, 6 and 7 when the horizontal distance is small and differ
246 significantly as the horizontal distance increases. These features of consistent local time variation and
247 close proximity with the true TEC over KWA further validates the accuracy of estimated V_a by single
248 station method. Hence, we conclude that the single station method described in section 3.2 is appropriate
249 for the estimation of absolute TEC for LEOS with low-inclination orbits, such as C/NOFS.

250 4. LSWS from longitudinal variation of TEC

251 The longitudinal variation of TEC often exhibits zonal wave-like structures, superimposed on the
252 background variation, which can be regarded as large scale wave structure (LSWS). Rottger [1973], from
253 transequatorial propagation experiment, has reported that the ESF patches were distributed quasi-
254 periodically in longitude and interspersed by an average zonal distance of about ~380 – 450 km. They
255 have interpreted these quasi-periodic ESF structures in east-west direction to the zonal wave lengths of
256 LSWS excited by atmospheric gravity waves. Tsunoda and White, [1981] from ALTAIR incoherent
257 scatter radar observations have shown that the zonal wave lengths of LSWS vary around ~300 – 600 km,
258 which were later supported by satellite in-situ observations by Singh et al., [1997]. Therefore, the
259 variations in TEC with scale lengths greater than 800 km can be safely assumed as the background
260 variation and may be subtracted from the longitudinal TEC variation in order to derive the zonal LSWS.
261 Thampi et al., [2009] and Tsunoda et al., [2010] have assumed that the mean IPP location sweeps through
262 to zonal distance of ~1000 km within 2.5 minutes period of observations from C/NOFS, hence computed
263 a 2.5 minute period running average of TEC and subtracted from the longitudinal TEC variation in order
264 to derive LSWS. However, care must be taken while subtracting the running average of a uniform time
265 interval owing to the fact that uniform time interval does not corresponds to a uniform zonal distance due
266 to the differential variation of satellite elevation angle during different epochs of satellite pass. This is
267 because, with respect to ground receiver, the satellite elevation angle (θ) varies slowly when the satellite
268 is far, varies rapidly at the closest approach, and again varies slowly as the satellite is moving away. For

269 example, Figure 5a shows the absolute change in θ per 1-sample ($\delta\theta$) as a function of time since the
 270 beginning of data acquisition for a C/NOFS pass at 1225 UT of 26 February 2011 from an equatorial
 271 station, Bac Lieu (BCL). Figure 5b shows the variation of zonal distance that corresponds to 2.5 minute
 272 (± 1.25 minute) time interval centered at that point of time. It can be seen from this figure that the
 273 variation in $\delta\theta$ is quite significant during the different epochs of the satellite pass and the corresponding
 274 zonal distance varies from 900 km to 500 km. Therefore, the running average of a uniform time interval
 275 is not suitable; instead one needs to subtract the running average of a uniform zonal scale size of 800 km.
 276 Hence, the process is refined here as described in the following lines. The zonal distance swept by the
 277 IPP at an altitude of 300 km computed and the variation of V_a (blue curve) as a function of zonal distance
 278 in shown in Figure 5c. The corresponding IPP longitudes are shown in the x-axis at the top. It can be
 279 observed from this figure that the zonal variation of V_a exhibits wave-like structures conspicuously to the
 280 east of 100°E longitude. It should be mentioned here that even though V_a curve is smooth because of fine
 281 spatial resolution, the sampling interval of zonal distance is not uniform as discussed previously.
 282 Therefore, the V_a curve is re-sampled at a uniform zonal distance of 1 km. Now the running average
 283 corresponding to 800 km is subtracted (red dashed line) from the V_a curve and the residual variations are
 284 shown in Figure 5d. While computing the 800 km running average curve (red dashed line), we applied
 285 the hamming window weighting function [Oppenheim and Schaffer, 1989] on the data series in order to
 286 reduce the edge effects at the beginning and end of the data series. It can be seen from the Figure 5d that
 287 the residual V_a exhibits zonal wave-like variations with wave lengths of ~ 250 to 615 km, which are
 288 consistent with the values reported for LSWS in earlier studies [Rottger, 1973; Tsunoda and White, 1981;
 289 Singh et al., 1997].

290 5. Discussion

291 The equatorial ionosphere often exhibits zonal wave-like structures that manifest as a quasi-
 292 periodic modulation in the height of iso-electron density contours by backscatter radar maps, which were
 293 termed as a Large Scale Wave Structure (LSWS) by Tsunoda and White [1981]; Tsunoda, [1981] and

294 Tsunoda et al., [2005]. They have further shown that the ESF irregularities or equatorial plasma bubbles
 295 (EPBs) grow from the upwellings or crests of LSWS. Figure 6 shows the zonal wave-like structures in
 296 the longitudinal variation of V_a simultaneously observed from three equatorial and low-latitude stations,
 297 BCL, HCM and NHA for the same C/NOFS pass as that shown in Figure 5. The top panel shows the
 298 locations of the three stations and the IPP tracks of C/NOFS pass for the three stations. The x-axis at the
 299 top represents the local times corresponding to the IPP longitudes. The vertical green and red dotted lines
 300 represent the location of sunset terminator corresponding to E-region (110 km) and F-region (200)
 301 altitudes. The second panel (Figure 6b) shows the variation of V_a (solid lines) from the three stations as a
 302 function of IPP longitude. It can be observed from this figure that the estimated V_a exhibits zonal wave-
 303 like structures for all the three stations, conspicuously to the east of 100°E longitude. The local times at
 304 the corresponding longitudes are post-sunset hours. The residual V_a variations after subtraction of 800 km
 305 running average curves (dotted lines in Figure 6b) are shown in Figure 6c.

306 It is interesting to observe that these zonal wave structures in the residual TEC (V_a) are closely
 307 aligned for the three stations which are separated by about 3.6° and their IPP tracks are separated by ~2.3°
 308 in dip latitude. This close alignment suggests that these zonal structures are in fact aligned with
 309 geomagnetic field (\vec{B}) lines at least for ~255 km since the declination angle of \vec{B} lines is nearly zero in this
 310 sector. Similar alignment was also evidenced from the earlier reports by Thampi et al. [2009] and
 311 Tsunoda et al. [2010]. Figure 6d shows the amplitude scintillations observed on both 150 and 400 MHz
 312 frequency signals from BCL receiver. The similar amplitude scintillations observed from HCM and NHA
 313 receivers are not shown for simplicity. Four distinct scintillation patches, labeled 1 to 4, occurred during
 314 this particular C/NOFS pass as can be observed from this figure. Most important result from this
 315 observation is that these four scintillation patches are aligned with the westward walls of residual TEC
 316 depletions as indicated with vertical dotted lines. Since the equatorial plasma bubbles (EPBs), which
 317 cause these scintillations, are known to be aligned to \vec{B} field lines, it is convincing to conclude that these
 318 zonal structures are actually aligned with \vec{B} field lines.

319 It was shown that the equatorial plasma bubbles (EPBs) grow from the upwellings or crests of the
320 LSWS [Tsunoda and White, 1981; Tsunoda, 1981 and Tsunoda 2005]. The upwellings develop in the
321 bottomside F-region when the low-density plasma is pushed upward locally, probably due to polarization
322 electric fields [Weber et al., 1978]. This is analogous to the upwelling in fluids due to buoyancy forces.
323 The upwellings appear as an upward push in the isoelectron density contours of incoherent scatter radar
324 maps when viewed in East-West plane. Since the low density plasma is pushed upward, the upwellings
325 manifest as depletions in residual TEC variations as seen in Figure 6c. Tsunoda and White [1981] and
326 Tsunoda [1983] have further shown, from the backscatter radar maps, that the EPBs initially develop at
327 the westward wall of upwellings. Thus, the alignment of scintillation patches with the westward walls of
328 residual TEC depletions (Figures 6c and 6d) further reinforces the findings of earlier studies on LSWS
329 and ESF [Tsunoda and White, 1981; Tsunoda 1981, 1983, 2005; Tsunoda et al., 2010, 2011 and Thampi
330 et al. 2009]. Therefore, based on above results, (i) zonal wavelengths in the range ~250 to 615 km, (ii)
331 the alignment of EPBs (scintillation) with the westward walls of upwellings (TEC depletions), and (iii)
332 their alignment with \vec{B} field lines, it can be concluded that these zonal wave-like structures observed in
333 Figure 6 are the large scale wave structure in the bottom side F-region. Thus, the differential phase
334 measurements from the beacon transmissions from low-inclination orbiting satellites fills a void in the
335 direct observations of LSWS, which to date, have been possible only with the ALTAIR radar.

336 A careful examination of the Figure 6c reveals the presence of wave like feature also westward of
337 100°E longitude, i.e., weaker wave structure appears to be present even before the E-region sunset (green
338 dotted line). Such a sequence, namely, pre-sunset wave structure increasing in amplitude towards post-
339 sunset hours when ESF structures may also evolve, has been reported earlier in F-layer heights by Abdu
340 et al., [2009] and in TEC by Tsunoda et al., [2010 and 2011]. This indicates that the initiation of LSWS
341 can appear even before the sunset due to the excitation of atmospheric gravity waves (AGW) in the
342 troposphere, their propagation up to thermosphere and transfer of AGW wind perturbations via neutral-
343 ion coupling to the plasma at the base of F-layer [Abdu et al., 2009; Tsunoda 2010 and Tsunoda et al.,

344 2011]. Abdu et al., [2009] have also reported the modulation of F-layer plasma distribution by AGW as
345 seen in its characteristic forms in F-layer heights observed by radar and Digisonde. The substantial
346 enhancement of LSWS amplitude during the post-sunset period indicates that the growth of LSWS is
347 aided by the polarization electric fields developed by the F-region dynamo after the sunset. The detailed
348 discussion on the atmospheric coupling processes leading to the excitation of LSWS by AGW and the
349 subsequent instability processes leading to the evolution of EPBs can be found in Tsunoda [2005, 2010],
350 Abdu et al., [2009] and Tsunoda et al., [2010, 2011].

351 6. Summary and Conclusions

352 A low-latitude network of radio beacon receivers, namely GRBR network, is currently
353 established around the Southeast Asia and Pacific regions by the joint efforts of RISH, Kyoto University
354 and SRI International, USA which is further planned to expand into Indian and African low latitudes.
355 The principal experiment involves differential phase measurements at spatially distributed locations from
356 dual/tri-band radio beacon transmitters onboard the LEOS to study the three dimensional structures of
357 ionospheric electron content by tomographic imaging and to investigate the atmospheric coupling
358 processes leading to the generation of ESF and scintillations. With the availability of beacon transmitters
359 onboard the LEOS in low-inclination orbits, such as CERTO beacon on C/NOFS, it is now possible to
360 determine the zonal (longitudinal) variation of ionospheric TEC with fine spatial resolution over a wide
361 longitudinal region. For low-inclination satellite passes, the initial TEC offset and absolute vertical TEC
362 can be accurately estimated using the single station observations described in section 3.2. By subtracting
363 the background variation (zonal wave lengths > 800 km), the LSWS can be successfully extracted from
364 the longitudinal variation of TEC. The zonal wave lengths of LSWS are found to vary around ~ 250 to
365 615 km. These zonal structures were found, in general, to be aligned with geomagnetic (\vec{B}) field lines
366 and scintillations are found to align with the westward wall of TEC depletions. The initiation of LSWS
367 by the AGW can be observed even before the sunset and its amplitude grows substantially during the
368 post-sunset periods, probably, aided by the polarization electric fields developed due to F-region dynamo.

369 These are the typical signatures of LSWS. Thus, the application of differential phase measurements for
370 determining the longitudinal plasma structures is an excellent diagnostic tool to study the characteristics
371 of LSWS and their source mechanisms on a regular basis. In this context, the low-latitude GRBR
372 network lays an excellent platform to study the LSWS, scintillations and their interrelationship to uncover
373 the processes leading to yet enigmatic day-to-day randomness of ESF.

374 Acknowledgements

375 The work of STR is supported by Japan Society for Promotion of Science (JSPS) Foundation.
376 This work was partly supported by Grant-in-Aid for Scientific Research (B) (22403011). Research by
377 RTT was supported by NSF grant ATM-0720396, and by AFOSR contract FA9550-10-C-0004. Satellite
378 receivers at HCM and NHA were part of collaboration with HCM Institute of Physics/VAST (Vietnam).
379 The work of ST is supported by Department of Space, Government of India. The C/NOFS (CINDI)-IVM
380 data are provided through University of Texas at Dallas supported by NASA grant NAS5-01068. The
381 authors acknowledge the open data policy of Kwajalein Digisonde data is through UML DIDBase
382 (<http://ulcar.uml.edu/DIDBase/>).

383 References

- Abdu, M. A., E. A. Kherani, I. S. Batista, E. R. de Paula, D. C. Fritts, and J. H. Sobral (2009), Gravity wave initiation of equatorial spread F/plasma bubble irregularities based on observational data from the SpreadFEx campaign, *Ann. Geophys.*, 27, 2607-2622.
- Aitchison, G. J. and K. Weekes (1959), Some deductions of ionospheric information from the observations of emissions from satellites 1957a2-I, *J. Atmos. Terr. Phys.*, 14, 236-243.
- Bernhardt, P. A., and C. L. Siefring (2006), New satellite-based systems for ionospheric tomography and scintillation region imaging, *Radio Science*, 41(5), doi:10.1029/2005RS003360, issn:0048-6604.
- Bernhardt, P. A., C. L. Siefring, I. J. Galysh and D. E. Koch (2010), A new technique for absolute total

- electron content determination using the CITRIS instrument on STPSat1 and the CERTO beacons on COSMIC, *Radio Science*, 45, RS3006, doi:10.1029/2009RS004243.
- Coley, W. R., R. A. Heelis, B. J. Holt, and C. R. Lippincott (2010), Ion temperature and density relationships measured by CINDI from the C/NOFS spacecraft during solar minimum, *J. Geophys. Res.*, 115, A02313, doi:10.1029/2009JA014665.
- Davies, K. (1980), Recent progress in satellite radio beacon studies with particular emphasis on the ATS-6 radio beacon experiment, *Space Sci. Rev.*, 25, 357-430.
- Garriott, O. K. (1960), The determination of ionospheric electron content and distribution from satellite observations Part 1. Theory of the Analysis, *J. Geophys. Res.*, 65(4), 1139-1150.
- Kersley, L., J.A.T. Heaton, S. E. Pryse, and T.D. Raymund (1993), Experimental ionospheric tomography with ionosonde input and EISCAT verification, *Ann. Geophysicae*, 11, 1064-1070.
- Kherani, E. A., M. A. Abdu, E. R. de Paula, D. C. Fritts, J. H. A. Sobral and F. C. de Meness Jr (2009), The impact of gravity waves rising from convection in the lower atmosphere on the generation and nonlinear evolution of equatorial bubble, *Ann. Geophys.*, 27, 1657-1668.
- Leitinger, R., G. Schmidt, and A. Tauriainen (1975), An evaluation method combining the differential Doppler measurements from two stations that enables the calculation of electron content of the ionosphere, *J. Geophys.*, 40, 201-213.
- Oppenheim, A.V., and R.W. Schafer (1989), *Discrete-Time Signal Processing*, Prentice-Hall, 447-448.
- Rottger, J. (1973), Wave-like structures of large-scale equatorial spread-F irregularities, *J. Atmos. Terr. Phys.*, 35, 1195-1196, doi:10.1016/0021-9169(73)90016-0.
- Saito, S., and T. Maruyama (2007), Large-scale longitudinal variation in ionospheric height and equatorial spread F occurrences observed by ionosondes, *Geophys. Res. Lett.*, 34, L16109, doi:10.1029/2007GL030618.

- Singh, S., F.S. Johnson, and R.A. Power (1997), Gravity wave seeding of equatorial plasma bubbles, *J. Geophys. Res.*, *102*, 7399.
- Thampi, S.V., M. Yamamoto, R.T. Tsunoda, Y. Otsuka, T. Tsugawa, J. Uemoto, and M. Ishii (2009), First observations of large-scale wave structure and equatorial spread *F* using CERTO radio beacon on the C/NOFS satellite, *Geophys. Res. Lett.*, *36*, L18111, doi:10.1029/2009GL039887.
- Tsunoda, R. T. (1981), Time evolution and dynamics of equatorial backscatter plumes, 1. Growth Phase, *J. Geophys. Res.*, *86*, 139-149.
- Tsunoda, R. T. (2008), Satellite traces: An ionogram signature for large-scale wave structure and a precursor for equatorial spread *F*, *Geophys. Res. Lett.*, *35*, L20110, doi:10.1029/2008GL035706.
- Tsunoda, R. T. (2010c), On equatorial spread *F*: Establishing a seeding hypothesis, *J. Geophys. Res.*, *115*, A12303, doi:10.1029/2010JA015564.
- Tsunoda, R. T., D. M. Bubenik, S. V. Thampi, and M. Yamamoto (2010), On large - scale wave structure and equatorial spread *F* without a post - sunset rise of the *F* layer, *Geophys. Res. Lett.*, *37*, L07105, doi:10.1029/2009GL042357.
- Tsunoda, R. T., M. Yamamoto, T. Tsugawa, T. L. Hoang, S. Tulasi Ram, S. V. Thampi, H. D. Chau, and T. Nagatsuma (2011), On seeding, large - scale wave structure, equatorial spread *F*, and scintillations over Vietnam, *Geophys. Res. Lett.*, *38*, L20102, doi:10.1029/2011GL049173.
- Tsunoda, R.T. (1983), On the generation and growth of equatorial backscatter plumes. 2. Structuring of the west walls of upwellings, *J. Geophys. Res.*, *88*, 4869.
- Tsunoda, R.T. (2005), On the enigma of day-to-day variability in equatorial spread *F*, *Geophys. Res. Lett.*, *32*, L08103, doi:10.1029/2005GL022512.
- Tsunoda, R.T., and B.R. White (1981), On the generation and growth of equatorial backscatter plumes—

1. Wave structure in the bottomside F layer, *J. Geophys. Res.*, 86, 3610.

Tsunoda, R.T., and D.M. Towle (1979), On the spatial relationship of 1-m equatorial spread-F irregularities and depletions in total electron content, *Geophys. Res. Lett.*, 6, 873.

Tsunoda, R.T., D.M. Bubenik, S.V. Thampi, and M. Yamamoto (2010), On large-scale wave structure and equatorial spread F without a post-sunset rise of the F layer, *Geophys. Res. Lett.*, 37, L07105, doi:10.1029/2009GL042357.

Tulasi Ram, S., S.-Y. Su, C. H. Liu, B. W. Reinisch, and L.-A. McKinnell (2009), Topside ionospheric effective scale heights (HT) derived with ROCSAT-1 and ground-based ionosonde observations at equatorial and midlatitude stations, *J. Geophys. Res.*, 114, A10309, doi:10.1029/2009JA014485.

Weber, E. J., J. Buchau, R.H. Eather, and S.B. Mende (1978), North-south aligned equatorial airglow depletions, *J. Geophys. Res.*, 83, 712.

Yamamoto, M. (2008), Digital beacon receiver for ionospheric TEC measurement developed with GNU radio, *Earth, Planets, Space*, 60, e21.

384

385

386
387

Figure Captions

388 Figure 1: The geographical distribution of GRBR Network. The stations shown in green are currently
389 installed and blue were planned for future installations.

390 Figure 2: Comparison of estimated initial TEC offsets (Ψ) and absolute vertical TEC (V_a) derived from
391 Leitinger's two station method and single station methods for two of C/NOFS passes at 0949
392 UT (left panels) and 1459 UT (right panels) on 9 March 2011. Top panels show the relative
393 slant (line-of-sight) TEC observed from Bac Lieu (BCL) and Ho Chi Minh City (HCM).
394 Middle panels show the V_a derived from two stations method (green and brown dotted lines for
395 BCL and HCM, respectively) and single station method (blue and red solid lines for BCL and
396 HCM, respectively). The V_a estimated by two station method by confining the region of
397 overlap to 92-102°E longitudes are also shown in right middle panels (blue and red dotted lines
398 for BCL and HCM, respectively). The unit for Ψ is TECu (10^{16} electrons/m²). Bottom panels
399 show the amplitude scintillations observed at 150 MHz (blue) and 400 MHz frequency radio
400 beacon signals from C/NOFS.

401 Figure 3: Longitudinal variation of V_a derived from single station method for nice successive C/NOFS
402 orbits covering the local times from dusk to dawn on 18 May 2011 over an equatorial station,
403 Kosrae (KOS). The x-axis for each panel is shown in terms of local times corresponding to the
404 longitudes shown at top.

405 Figure 4: (a) The location of Kosrae (KOS) and Kwajalein (KWA) and the tracks of ionospheric pierce
406 points (300 km) for nine C/NOFS orbits on 18 May 2011. (b) The local time variations of V_a
407 (blue curve) and ITEC (red curve) corresponding to 167.2°E longitude sector. The vertical bars
408 represent the horizontal distance (right hand side scale) between the observational locations of
409 V_a and KWA.

410 Figure 5: Derivation of LSWS from the longitudinal variation of absolute vertical TEC (V_a). (a) Absolute
 411 change in satellite elevation angle ($\delta\theta$) per 1-sample as a function of time since the beginning
 412 of data acquisition. (b) Variation of zonal distance corresponding to 2.5 minute (± 1.25
 413 minutes) time interval centered at that point of time. (c) Variation of V_a (blue curve) as
 414 function of zonal distance (x-axis at bottom) and IPP longitude (x-axis at top) and 800-km
 415 running average curve (red dashed line). (d) Residual TEC variations showing the typical zonal
 416 wave lengths of $\sim 250 - 615$ km.

417 Figure 6: A typical example showing the zonal large scale wave structure and amplitude scintillations on
 418 26 February 2011. (a) IPP tracks for three stations, BCL, HCM and NHA, (b) Longitudinal
 419 variation of V_a (solid line) and 3-min running average (dotted lines) curves for the three stations,
 420 (c) The residual TEC variations, (d) Amplitude scintillations and (e) S4-index at 150 and 400
 421 MHz observed over BCL. The vertical green and red dotted lines represent the location of
 422 sunset terminator corresponding to E-region (110 km) and F-region (200) altitudes. The x-axis
 423 at the top represents the local times at the corresponding longitudes.

424

Table 1: Low-latitude GRBR Network

425

426

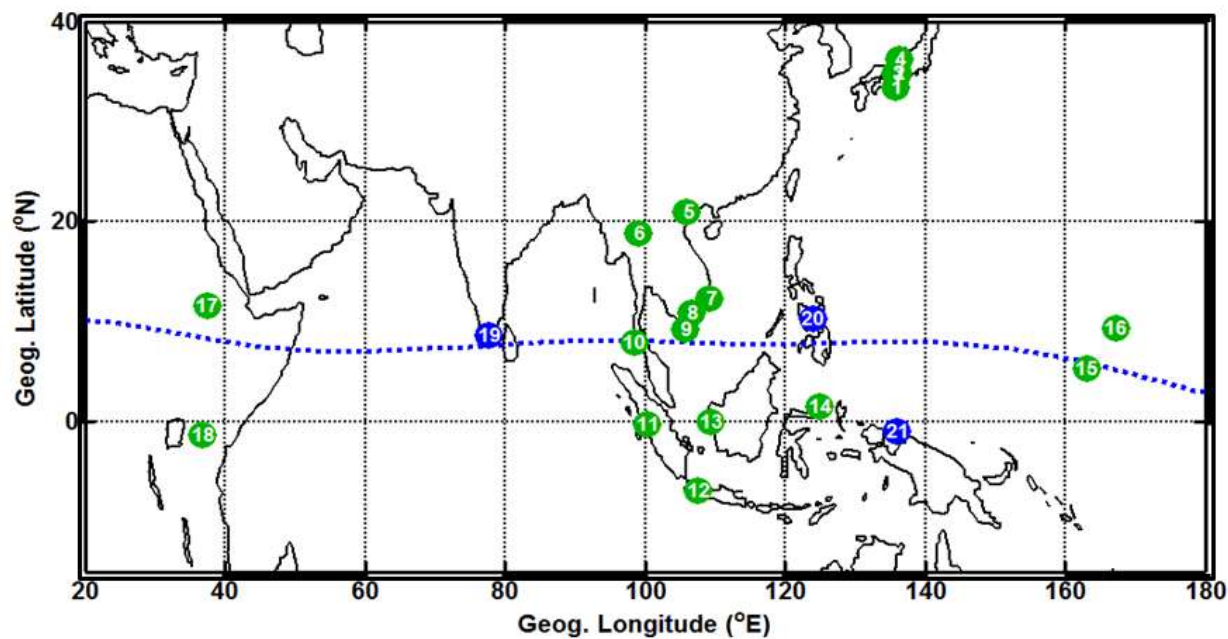
| <i>Station No.</i> | <i>Station Name</i> | <i>Station Code</i> | <i>Geog. Latitude</i> | <i>Geog. Longitude</i> | <i>Dip. Latitude</i> |
|---|-----------------------|---------------------|-----------------------|------------------------|----------------------|
| <i>Currently installed</i> | | | | | |
| 1 | Shionomisaki | SNM | 33.45 | 135.76 | 27.9 |
| 2 | Shigaraki (MUR site) | MUR | 34.85 | 136.1 | 29.43 |
| 3 | Uji | UJI | 34.90 | 135.8 | 25.53 |
| 4 | Fukui | FUK | 36.26 | 136.23 | 31.00 |
| 5 | Phuthuy | PHT | 21.03 | 105.96 | 15.75 |
| 6 | Chiang Mai | CMU | 18.79 | 98.92 | 13.03 |
| 7 | Nha Trang | NHA | 12.27 | 109.20 | 5.24 |
| 8 | Ho Chi Minh City | HCM | 10.85 | 106.56 | 3.52 |
| 9 | Bac Lieu | BCL | 9.29 | 105.71 | 1.67 |
| 10 | Phuket | PTC | 7.89 | 98.39 | -0.15 |
| 11 | Kototabang (EAR site) | EAR | -0.20 | 100.32 | -9.92 |
| 12 | Bandung | BDG | -6.89 | 107.59 | -17.66 |
| 13 | Pontianak | PTK | -0.00 | 109.36 | -9.19 |
| 14 | Manado | MND | 1.53 | 124.91 | -7.01 |
| 15 | Kosrae | KOS | 5.33 | 163.01 | -0.5 |
| 16 | Kwajalein | KWA | 9.40 | 167.2 | 4.3 |
| 17 | Bahirdar | BDU | 11.56 | 37.38 | 3.93 |
| 18 | Nairobi-KP | NKP | -1.28 | 36.81 | -12.05 |
| <i>Planned for future installation</i> | | | | | |
| 19 | Tirunelveli | ---- | 8.7 | 77.7 | 0.9 |
| 20 | Cebu | ---- | 10.35 | 123.91 | 3.09 |
| 21 | Biak | ---- | -1.0 | 136 | -9.68 |

427

428

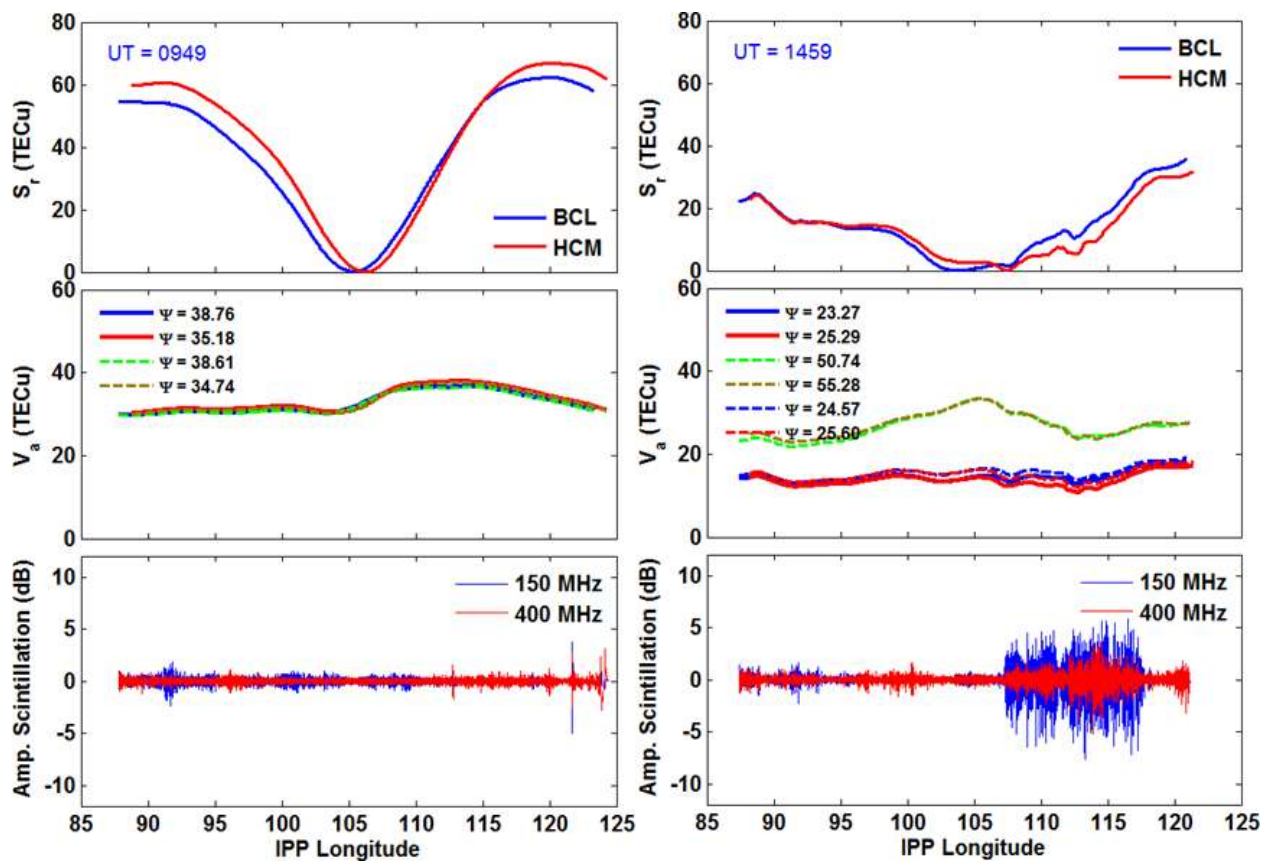
429

430 Figure - 1



431

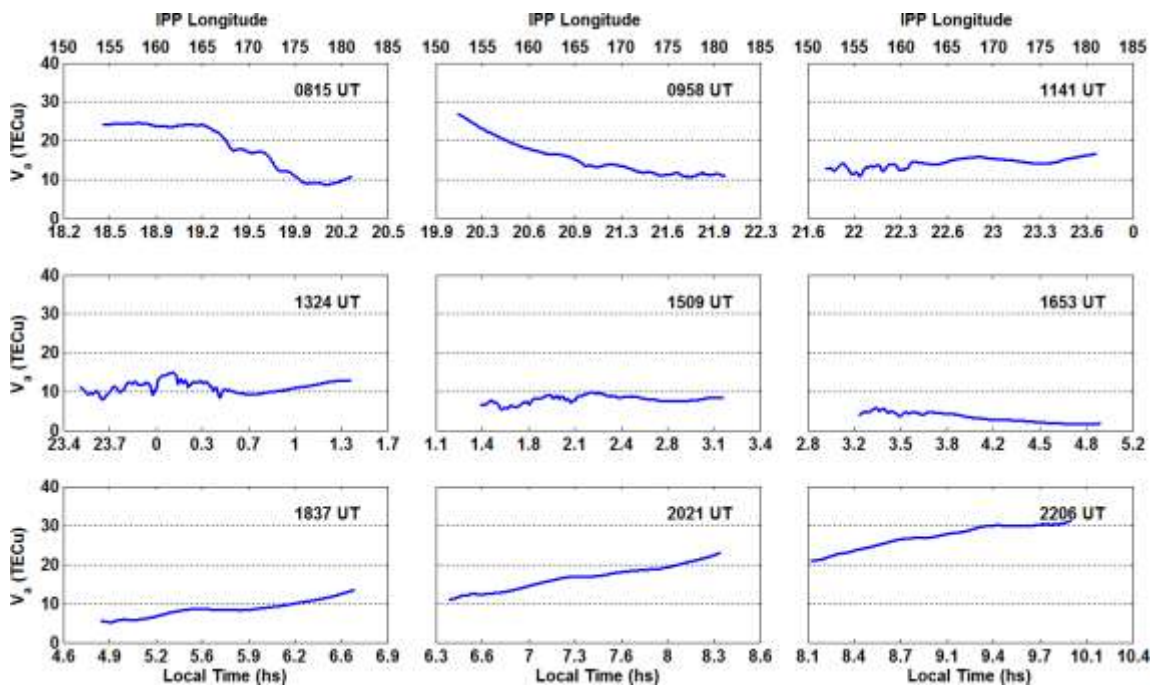
432 Figure - 2



433

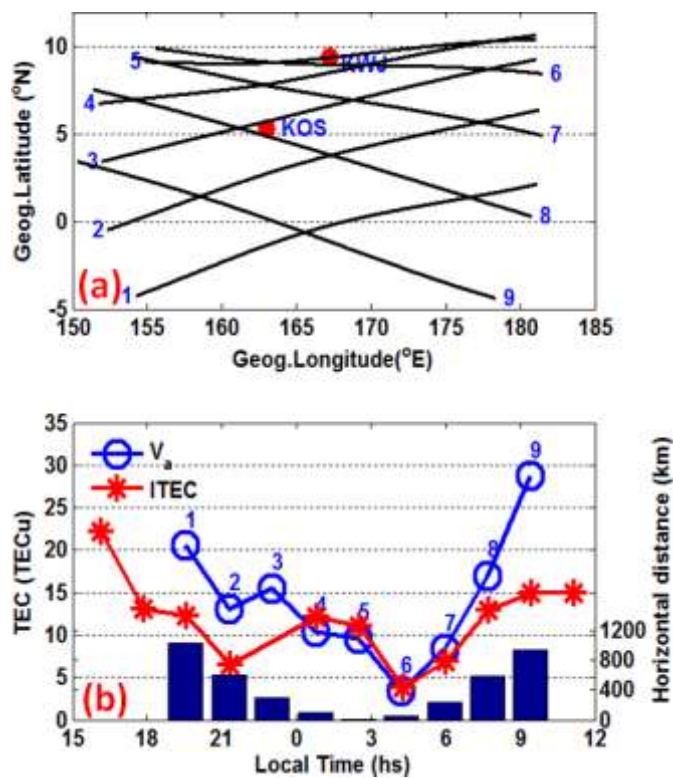
434

435 Figure – 3



436

437 Figure – 4



438

439

440

441

442

443

444

445

446

447

448

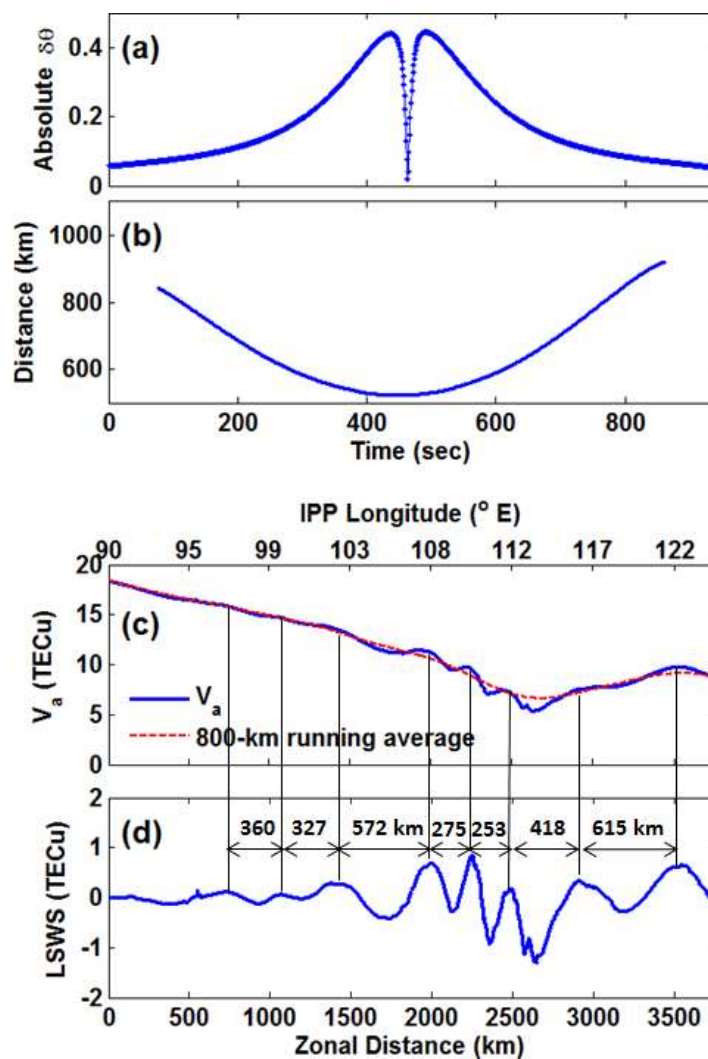
449

450

451

452

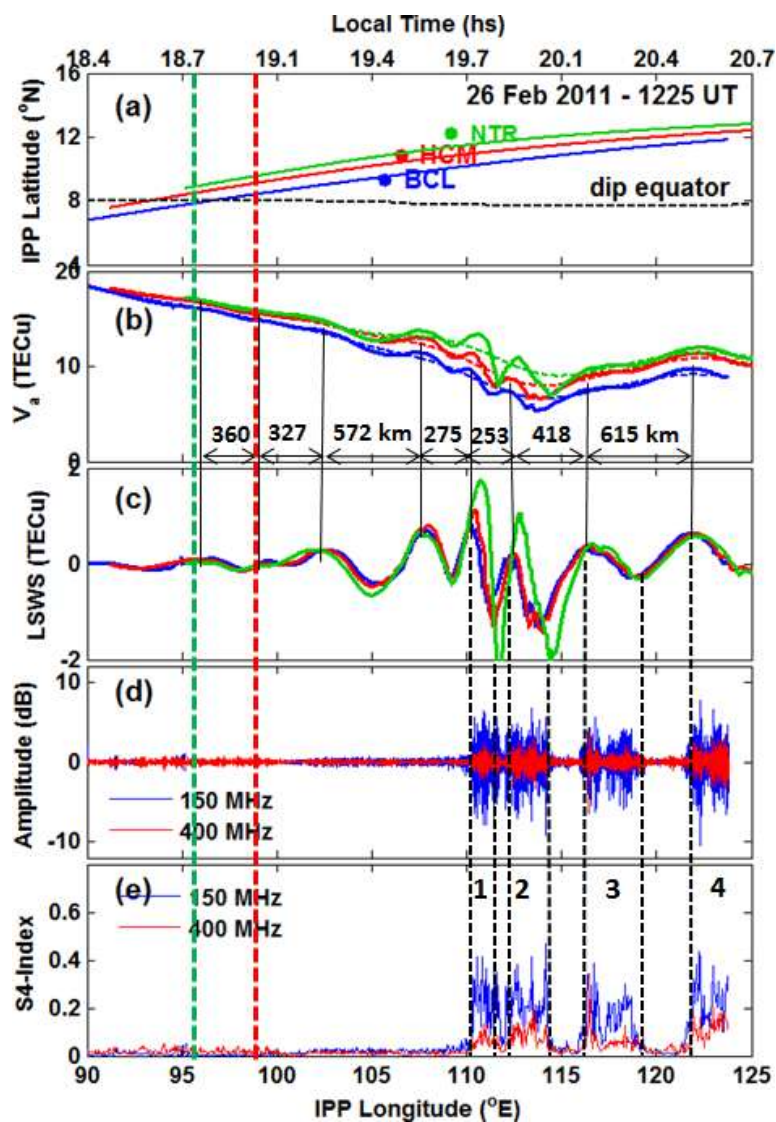
453 Figure – 5



454

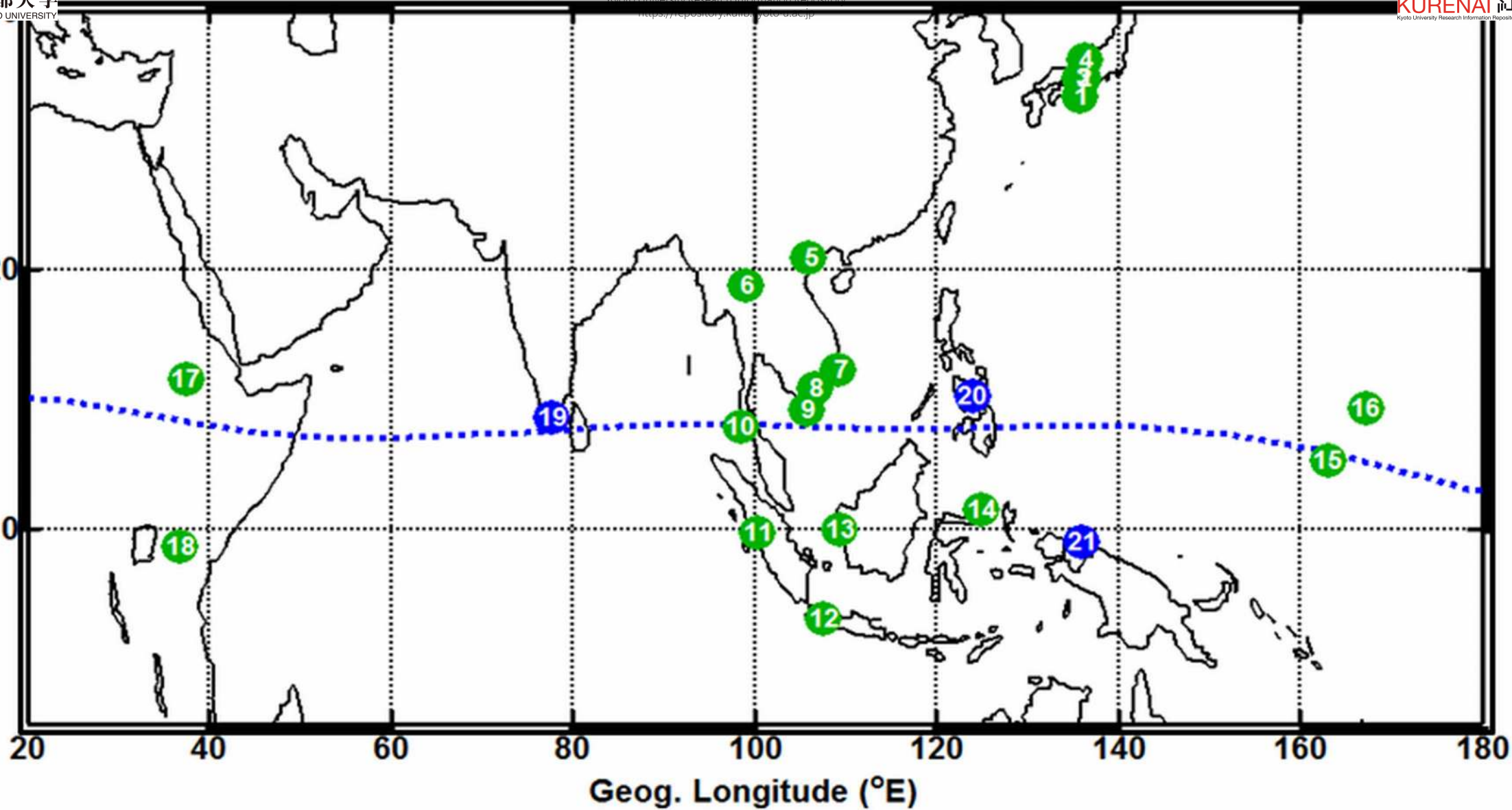
455

456 Figure 6



457

Geog. Latitude ($^{\circ}$ N)



Geog. Longitude ($^{\circ}$ E)

